J. Fluid Mech. (2019), *vol.* 864, *pp.* 273–285.
doi:10.1017/jfm.2019.40

Flow-induced motions of flexible plates: fluttering, twisting and orbital modes

Yaqing Jin[1], Jin-Tae Kim[1], Shifeng Fu[1,2] and Leonardo P. Chamorro[1,3,4,†]

[1]Mechanical Science and Engineering Department, University of Illinois, Urbana, IL 61801, USA

[2]College of Water Conservancy and Hydropower Engineering, Hohai University, Nanjing 210024, China

[3]Civil and Environmental Engineering Department, University of Illinois, Urbana, IL 61801, USA

[4]Aerospace Engineering Department, University of Illinois, Urbana, IL 61801, USA

(Received 28 October 2018; revised 2 December 2018; accepted 6 January 2019;
first published online 7 February 2019)

The unsteady dynamics of wall-mounted flexible plates under inclined flows was fundamentally described using theoretical arguments and experiments under various Cauchy numbers $Ca = \rho_f bL^3 U_0^2/(EI) \in [7, 81]$ (where ρ_f is the fluid density, b and L are the plate width and length, U_0 is the incoming velocity, E is Young's modulus and I is the second moment of the area) and inclination angles α. Three-dimensional particle tracking velocimetry and a high-resolution force sensor were used to characterize the evolution of the plate dynamics and aerodynamic force. We show the existence of three distinctive, dominant modes of tip oscillations, which are modulated by the structure dynamic and flow instability. The first mode is characterized by small-amplitude, planar fluttering-like motions occurring under a critical Cauchy number, $Ca = Ca_c$. Past this condition, the motions are dominated by the second mode consisting of unsteady twisting superimposed onto the fluttering patterns. The onset of this mode is characterized by a sharp increase of the force fluctuation intensity. At sufficiently high Ca and α, the plate may undergo a third mode given by large-scale tip orbits about the mean bending. Using the equation of motion and first-order approximations, we propose a formulation to estimate Ca_c as a function of α; it exhibits solid agreement with experiments.

Key words: flow–structure interactions

1. Introduction

Flow-induced, unsteady dynamics of flexible objects is a ubiquitous phenomenon. Characterization and quantification of the dominant modes of oscillation and the distinctive coupling between flow and structures remain as longstanding open problems. Substantial investigations have focused on understanding the mechanisms modulating the mean bending and drag reduction of wall-mounted elastic structures. Body deformation modifies the drag scaling $F \propto U^2$ common in rigid counterparts to $\propto U^{2+V}$, where U is the flow velocity and V is the so-called Vogel exponent. For large flow velocity, $V = -2/3$, and slender structures typically exhibit quasi-parabolic

† Email address for correspondence: lpchamo@illinois.edu

deformation (Alben, Shelley & Zhang 2002, 2004). The effects of other factors, including buoyancy (Luhar & Nepf 2011), skin friction (Bhati *et al.* 2018) and mean shear of incoming velocity (Leclercq & De Langre 2016), have also been explored recently to estimate structure reconfiguration. Schouveiler & Boudaoud (2006) investigated the deformation of a radially cut disk and formulated a model that matched very well the disk drag; it predicts $V = -4/3$ under sufficient deformation.

Flow instability may modulate body oscillations around the equilibrium bending. Such phenomenon has been extensively explored for the cases of flexible filaments parallel to uniform flows; distinctive, high-amplitude flapping motions may be triggered in individual and tandem configurations (Alben & Shelley 2008; Jia & Yin 2008; Ristroph & Zhang 2008; Kim, Huang & Sung 2010; Uddin, Huang & Sung 2013). Comparatively, flow-induced oscillations of wall-mounted elastic plates facing a flow are usually less distinctive. Despite the fact that wake fluctuations may induce unsteady force on bent structures, the unsteady force is usually a relatively small fraction of the mean drag (Luhar & Nepf 2011) and a secondary factor in determining the structure posture. In those configurations, the plate oscillations may be strongly dominated by the natural frequency, whereas distinctive Kármán vortex shedding may modulate the wake fluctuations (Jin, Kim & Chamorro 2018*a*; Jin *et al.* 2018*b*).

In nature and engineering applications, structures can often be inclined with respect to the incoming flow. Aero/hydrodynamic loads and wake characteristics are significantly influenced by the angle of attack (Fage & Johansen 1927; Modi *et al.* 1992; Amandolese, Michelin & Choquel 2013). Experimental investigations by Lam (1996) and Lam & Leung (2005) showed the distinctive vortex shedding from inclined rigid plates. Trailing-edge vortices were found to induce more fluid circulation and production of Reynolds stress compared to the leading-edge vortices. Inclined structures produce asymmetric wakes and net aero/hydrodynamic torque on the plate, which may trigger complex rotation or pitching motions dependent on the incoming velocity, plate geometry and structure stiffness (Iversen 1979; Mirzaeisefat & Fernandes 2013; Onoue *et al.* 2015; Jin *et al.* 2016). A recent study by Onoue *et al.* (2015) reported that the pitching amplitude of a rigid flat plate may exhibit hysteresis and abrupt changes as a function of structure torsional stiffness. Despite this common scenario, the physics modulating the dynamics of wall-mounted inclined flexible plates has not been uncovered.

In this study, we explore such phenomena using theoretical arguments and carefully designed laboratory experiments. We describe three dominant, distinctive modes of plate oscillations, namely, fluttering, twisting and orbital motions. We also show that the intensity of force fluctuations increases significantly past a critical condition, which coincides with the transition from small-amplitude fluttering to twisting. The experimental results and theoretical formulation offer a framework to characterize complex structure motions under flows with arbitrary direction, and insight on the aerodynamic load of elastic structures under a variety of flow fields. The paper is organized as follows: the experimental set-up is elaborated in § 2, the results and analysis are discussed in § 3, and conclusions are provided in § 4.

2. Experimental set-up

Selected laboratory experiments were conducted in the free-stream region of the Talbot wind tunnel at the University of Illinois. The wind tunnel has a test section 6 m long, 0.46 m high and 0.914 m wide; see details of the facility in Adrian, Meinhart

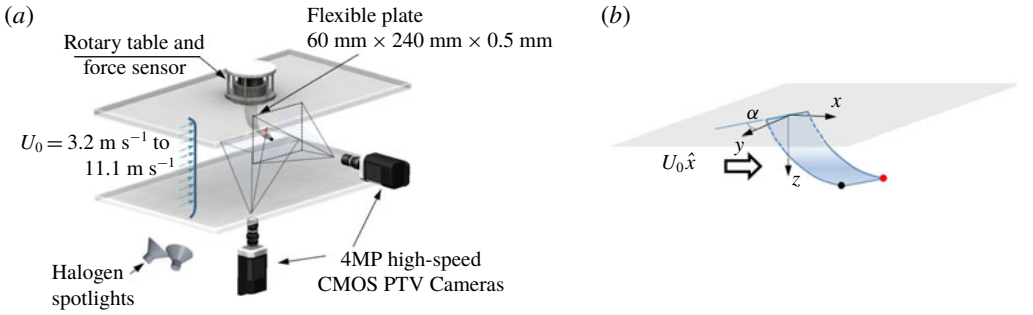

FIGURE 1. (Colour online) (*a*) Schematic of the experimental set-up illustrating the force sensor, rotary table and PTV system. (*b*) Basic definitions; the origin of the coordinate system is fixed at the centre of the plate base, the black and red fiducial points denote the tips used in other figures, and α is the inclination angle at the plate base with respect to the mean flow U_0.

& Tomkins (2000). A flexible flat plate made of acrylic was mounted over a Velmex rotary table and vertically hung from the top wall of the wind tunnel as a cantilever beam (figure 1*a*). The elastic plate was fixed near the entrance of the wind tunnel, at 0.7 m from the inlet, where the boundary layer effects are negligible. The plate has a height $L = 240$ mm, width $b = 60$ mm, thickness $c = 0.5$ mm, Young's modulus $E = 2.4$ GPa and density $\rho_m = 1180$ kg m^{-3}. The high mass ratio $\rho_m/\rho_f \approx 10^3$ ensured minor influence of the added mass in the structure dynamics. The unsteady dynamics of the plate was characterized at 35 incoming velocities $U_0 \in [3.2, 11.1]$ m s^{-1} every $\Delta U_0 \approx 0.23$ m s^{-1}, resulting in Reynolds numbers $Re = U_0 b/\nu \in [1.3, 4.4] \times 10^4$, or Cauchy numbers $Ca = \rho_f b L^3 U_0^2/(EI) \in [7, 81]$ (Lu *et al.* 2016); here $I = bc^3/12$. For each velocity, the plate was placed at an inclination angle $\alpha = 0°$, 30° and 45° controlled by the rotary table with an accuracy of 100 arcsec. The angle $\alpha = 0°$ refers to the plate facing the incoming flow (see figure 1*b*).

The instantaneous flow-induced force acting on the elastic plate was measured at a frequency of 1 kHz for periods of 30 s using a high-resolution ATI Gamma load cell connected at the plate base, which was mounted outside of the test section (Jin & Chamorro 2017; Jin, Hayat & Chamorro 2017). The dynamics of the plate tips was tracked using a three-dimensional (3D) particle tracking velocimetry (PTV) system at a frequency of 300 Hz for periods of 30 s with camera views at the bottom and one side of the plate to track instantaneous 3D motions (figure 1*a*). The plate was illuminated with two Stanley lithium ion halogen spotlights and captured within an investigation volume of 240 mm × 160 mm × 160 mm using two 4 MP Mikrotron EoSens 4CXP MC4082 high-speed cameras. Nikon AF Micro-Nikkor 50 mm lens with a focal ratio $f/2.8$ were used to maximize the focus on the selected investigation volume. The centroid of illuminated fiducial points was detected at subpixel level and tracked using the Hungarian algorithm and linked by performing a three-frame gap closing to obtain linked trajectories. A robust calibration is required to minimize the position error of detected points. The investigation volume was calibrated using a 200 mm × 200 mm planar target containing 342 fiducial points placed 10 mm apart. The root mean square (r.m.s.) of the recognized calibration points was $\approx 2 \times 10^{-4} L$. The calibration process was performed for each case by carefully placing the calibration target in the vicinity of the plate oscillation centre to account for the change in pixel/millimetre ratio along the camera view. To further

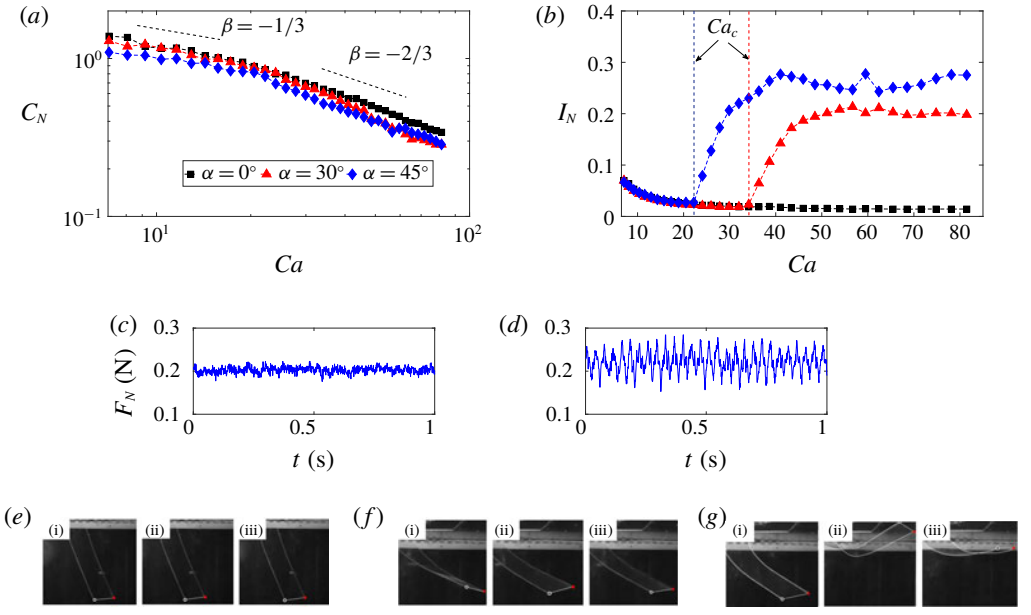

FIGURE 2. (Colour online) (*a*) The normal-force coefficient (C_N) for various Ca and α. (*b*) Intensity of the normal-force fluctuations (I_N) across various Ca and α. (*c*,*d*) Sample time series of the normal force F_N at the plate base right below ($Ca = 20.5$ for panel *c*) and above ($Ca = 24$ for panel *d*) Ca_c at $\alpha = 45°$. (*e–g*) Snapshots of plate dynamics at $\alpha = 45°$ and various Ca: (*e*) $Ca = 9$, (*f*) $Ca = 32$ and (*g*) $Ca = 68$. Here (i), (ii) and (iii) are instants highlighting dominant modes of tip motion.

reduce the error of velocity estimation, the PTV data were smoothed by using the least-squares spline method. More details about the PTV set-up can be found in Kim *et al.* (2016). To minimize any initial transient effect, the force fluctuations and tip motions were sampled after the steady state was reached (waiting time of at least 60 s).

3. Results

3.1. *Aerodynamic force fluctuations and plate dynamics*

Characterization of the plate motions and fluctuations of the aerodynamic force across Ca and α revealed distinctive patterns. First, quantification of the normal-force coefficient $C_N = 2F_N/(\rho_f U_0^2 bL)$ is illustrated in figure 2(*a*); here, F_N is the force component normal to the plate base. Despite the large variation of the inclination angle α, the trends of C_N as a function of Ca are comparable. For $Ca \lesssim 20$ one has $C_N \propto Ca^{-1/3}$ and for $Ca \gtrsim 20$ one has $C_N \propto Ca^{-2/3}$, corresponding to Vogel exponents of $V = -2/3$ and $-4/3$. Similar results were noted by Gosselin, De Langre & Machado-Almeida (2010) on flexible rectangular plates (their figure 5), indicating that strong plate deformation may alter the interaction mechanism between the plate and flow. Bulk quantification of the plate dynamics can be obtained with the intensity of the force fluctuations. In particular, distributions of the component normal to the base of the plate I_N ($= 2\sigma_N/(\rho_f U_0^2 bL)$, where σ_N is the standard deviation of F_N) as a function of Ca are illustrated in figure 2(*b*). It shows negligible differences between plate inclinations for sufficiently low Ca, and abrupt increase of the force fluctuations

past a critical $Ca = Ca_c$ threshold that depended on the inclination angle. Such a critical condition occurred at $Ca_c = 34$ and 22 for $\alpha = 30°$ and 45° cases, but it was absent at $\alpha = 0°$. To highlight the sharp change on the force fluctuations, figure 2(*c*,*d*) illustrates a sample time series of the normal force at the plate base F_N for the case $\alpha = 45°$ right before ($Ca = 20.5$) and after ($Ca = 24$) Ca_c. Despite the similar averaged values, distinctive high-amplitude periodic oscillations occurred right within $Ca > Ca_c$ implying the onset of a different oscillation mode. This is also consistent with recent work by Leclercq, Peake & de Langre (2018), where plate motions had a minor influence on the time-averaged flow-induced loads.

The instantaneous snapshots shown in figure 2(*e–g*) provide a basic linkage of the force fluctuation and distinctive dynamics of the plate motions for the particular case with $\alpha = 45°$. At $Ca < Ca_c$ (figure 2*e*), the plate exhibited small-amplitude fluttering around the bending equilibrium. The increase of Ca over Ca_c (figure 2*f*) resulted in twisting oscillations around a relatively larger bending. At sufficiently high Ca, the plate tips exhibited comparatively large-scale orbital motions; this condition happened at $Ca \gtrsim 43$ ($\alpha = 45°$). There, the tip was dominated by anticlockwise orbits coupled with twisting oscillations, as illustrated in figure 2(*g*). See additional details in the supplementary movies available at https://doi.org/10.1017/jfm.2019.40.

The trajectories of the tip motions for various Ca and α illustrate the dominant modes of oscillation. Indeed, figure 3(*a–c*) shows minor fluttering corresponding to low I_N around the bending equilibrium for $\alpha = 0°$. Such a mode is also observed under $\alpha = 30°$ and 45° within $Ca < Ca_c$ (figure 3*d*,*g*). At Ca_c, the plate experienced the onset of twisting oscillations. This resulted in stronger tip motions and, consequently, increased I_N (figure 3*e*,*f*,*h*,*i*). As expected, the intensity of tip oscillations increased with Ca and α. Dominant 3D orbital motions occurred at a specific threshold, which is the case in figure 3(*i*) at $Ca = 68$ and $\alpha = 45°$. It is worth noting that such 3D dynamics led to significant deviations of the plate tips from the bending equilibrium; in this case the orbits from each tip overlapped.

Specific insight on the distinctive modes of oscillation is obtained by examining the representative trajectories and spectra of the tip velocity. In the fluttering-like mode, the bending deformation dominates the reconfiguration of the elastic plate where the tip is nearly parallel to the base. As noted in figure 4(*a*), the streamwise velocity spectrum Φ^* of one of the tip edges evidences the modulation of the first- and second-order natural frequencies of the bending; these are given by $f_{b,r} = (j_r/L^2)\sqrt{EI/(\rho_m bc)}$, where $j_1 = 0.56$ and $j_2 = 3.51$. As reported in previous works (Fage & Johansen 1927; Modi *et al.* 1992; Onoue *et al.* 2015; Liu *et al.* 2017), for a thin flat plate inclined with respect to the mean flow, the aerodynamic load produces a torque M that tends to twist the frontal surface perpendicular to the free-stream flow. Its magnitude is given by

$$M = \tfrac{1}{2} C_M(\alpha)\rho_f U_e^2 A b, \tag{3.1}$$

where $C_M(\alpha)$ is the moment coefficient, U_e is the effective wind speed and A represents a characteristic area of the structure. An increase of the velocity results in an increment of the torque and the likelihood of tip twisting, which is controlled by the body stiffness. Such modulation, however, is continuously disturbed by the wake fluctuations resulting in twisting oscillations (figure 4*b*). The height difference between the tips (Δz_t^*) leads to the tip not being parallel to the base. In such cases, the tip velocity was substantially higher than the fluttering-like mode and exhibited semi-periodic variations. This is reflected by the dominating frequency component f_t in the spectral domain. It is worth noting that f_t remains nearly constant within all

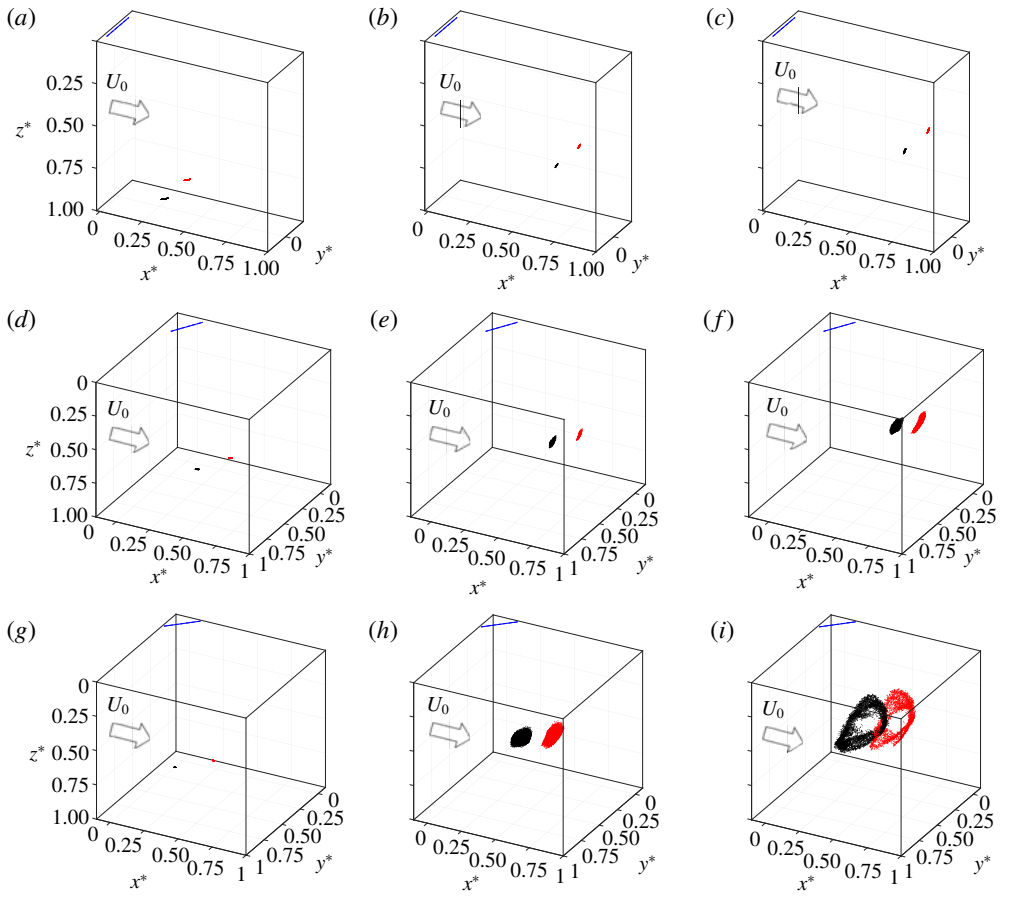

FIGURE 3. (Colour online) Trajectories of the tips for various α and Ca: (*a–c*) $\alpha = 0°$ with $Ca = 7$, 41 and 68; (*d–f*) same as (*a–c*) with $\alpha = 30°$; (*g–i*) same as (*a–c*) with $\alpha = 45°$. Here $x^* = x/L$, $y^* = y/L$ and $z^* = z/L$ denote the normalized tip locations. The blue lines represent the location of the plate base.

the twisting configurations, indicating that it is determined only by the characteristics of the structure.

Unlike the abrupt occurrence of the twisting mode from fluttering with Ca, the transition from twisting to 3D orbits is comparatively a gradual process, where I_N remains approximately constant. Indeed, the gradual development of the orbital motions may be noted from the changes on the normalized spectra Φ_N^* of the base normal force F_N with Ca (figure 5). Within the transition between twisting and orbital modes, the twisting mode f_t dominates the force fluctuations, whereas the signature of the orbital motions, f_r, exhibits a monotonic increase with Ca. In such a process, the force fluctuation intensity $\sigma_N^2 = \int \Phi \, \mathrm{d}f$ does not show abrupt changes due to the very similar Φ distributions across Ca. The corresponding tip dynamics in the transition to orbital motions is illustrated with tip trajectories in figure 4(*c*) at $Ca = 41$ and $\alpha = 45°$. It is characterized by twisting and 3D orbital motions. The associated tip velocity spectrum also reveals a dominant effect of the twisting mode (f_t) and the orbital motion f_r. The distinctive mode of orbital motions is observed

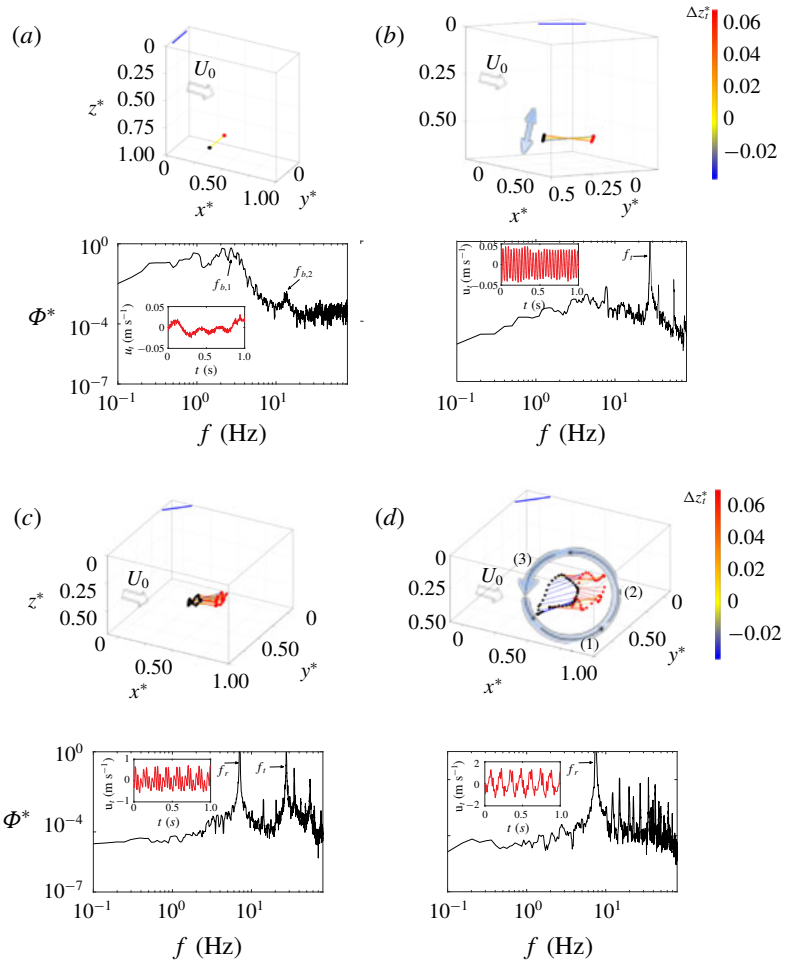

FIGURE 4. (Colour online) Sampled tip trajectories and normalized streamwise velocity spectra $\Phi^* = \Phi/\max\{\Phi\}$ of a tip under (*a*) $Ca = 7$ and $\alpha = 0°$, (*b*) $Ca = 41$ and $\alpha = 30°$, (*c*) $Ca = 41$ and $\alpha = 45°$, and (*d*) $Ca = 68$ and $\alpha = 45°$. The colour bar indicates the normalized height difference between the tips (Δz_t^*). The two-headed blue arrow in (*b*) denotes the twisting oscillations, whereas the anticlockwise arrow in (*d*) indicates the 3D orbital motion of the tips composed of three stages. The insets show the (red) tip streamwise velocity u_t.

only under $\alpha = 45°$ and $Ca \gtrsim 43$, which is a result of the coupling between plate twisting and bending as a three-stage process illustrated in figure 4(*d*) and figure 6 with instantaneous tip heights. The flow-induced torque at sufficiently high Ca and α leads to distinctive twisting of the plate near the tip such that the local projected area to the incoming flow increases (stage 1); this induces an abrupt increase of the aerodynamic load in the vicinity of the tip and substantial structure bending as highlighted by the decrease of z^* of both tips (stage 2). As depicted in figure 2(*f*,ii), relatively high load can substantially deform the elastic plate; local bending angle of the plate near the tip relative to the vertical axis can reach or even be larger than 90°. In this scenario (stage 3), the tip aerodynamic load drops significantly due to

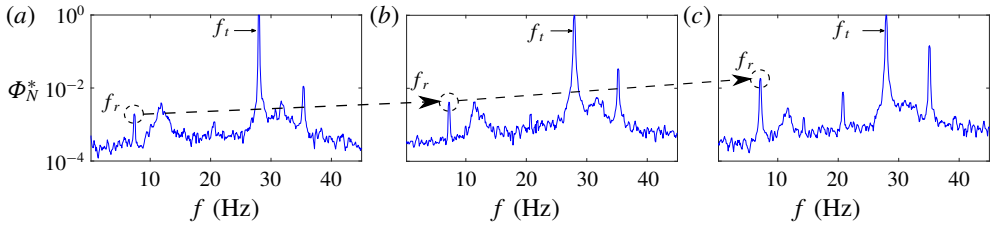

FIGURE 5. (Colour online) Normalized base normal-force spectra $\Phi_N^* = \Phi/\max\{\Phi\}$ at $\alpha = 45°$ and (*a*) $Ca = 36.3$, (*b*) $Ca = 38.6$ and (*c*) $Ca = 41$. The dashed arrows indicate the gradual increase of the frequency component corresponding to the orbital motions.

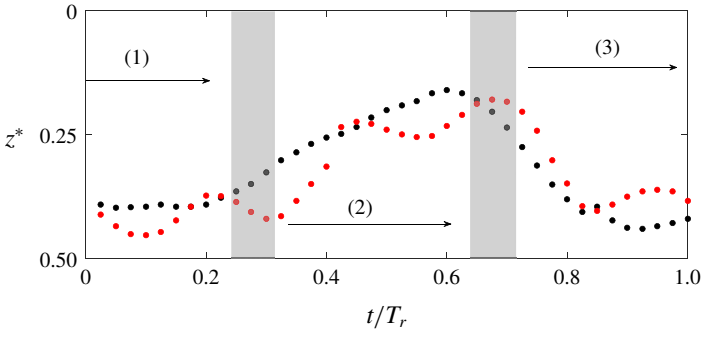

FIGURE 6. (Colour online) Instantaneous tip heights $z^* = z/L$ during one representative orbital cycle under $Ca = 68$ and $\alpha = 45°$; here $T_r = 1/f_r$ is the period of orbital motion. The black and red points denote each tip.

the reduced projected area. The structure restoring force governs the motion of the plate, pushing the tip back to the posture at stage 1, which completes an orbital cycle. Similar to the twisting mode, f_r is independent of Ca within the inspected configurations, despite the significant variation of the intensity of the orbital motions.

3.2. *Theoretical estimation of the critical Ca or Ca_c*

An uncovered key quantity is the threshold Ca_c that defines the condition of abrupt increase of force fluctuations leading to substantial unsteady loading. The aerodynamic load of an elastic structure undergoing simultaneous bending and twisting involves a number of physical processes. To tackle this problem quantitatively, we consider that the plate experiences minor deformation in a portion close to the tip. This assumption is well supported by the tracking of plate postures under $Ca < Ca_c$ (figure 2*d*) and previous studies (Schouveiler, Eloy & Le Gal 2005). Also, the plate dynamics shows that the plate remains nearly parallel to its base before the occurrence of the twisting mode. Hence, as a first-order approximation, we focus our analysis on the plate tip region with a constant local bending angle (θ) and inclination angle α relative to the free-stream flow at equilibrium, as illustrated in figure 7(*a*). There, the governing equation of the twisting dynamics of the plate can be characterized by

$$I_w \frac{\mathrm{d}^2\hat{\alpha}}{\mathrm{d}t^2} + c_w \frac{\mathrm{d}\hat{\alpha}}{\mathrm{d}t} + k_w\hat{\alpha} = -\frac{1}{2} C_M\Big|_{\hat{\alpha}_e} \rho_f U_e^2 A b, \tag{3.2}$$

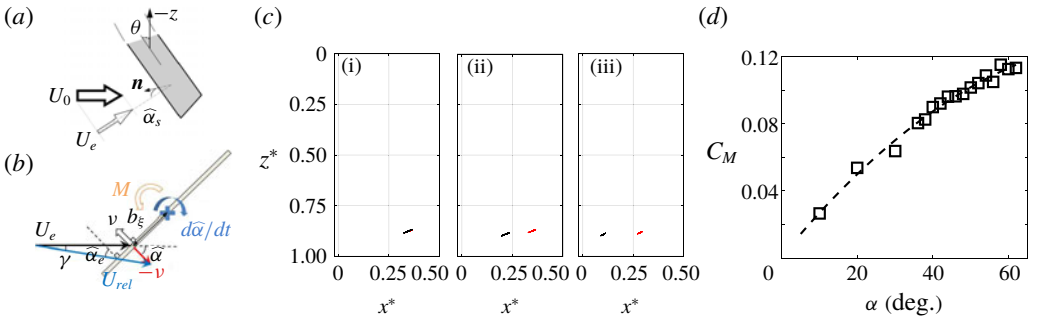

FIGURE 7. (Colour online) (*a*) Schematic illustrating parameters near plate tip region with bending angle θ. (*b*) Schematic of the cross-section of the plate undergoing twisting motion under the influence of instantaneous angular velocity. The '+' symbol denotes the plate centre. (*c*) Distribution of the plate tips projected in the x–z plane under $Ca = 7$ and (i) $\alpha = 0°$, (ii) $\alpha = 30°$ and (iii) $\alpha = 45°$. (*d*) Distribution of $C_M = 2M/(\rho_f U_0^2 b^2 L)$ with α of a rigid plate with the same geometry.

where $\hat{\alpha}$ is the modified inclination angle due to plate bending, I_w, c_w and k_w represent the polar moment of inertia, damping coefficient and torsional stiffness corresponding to the section under inspection, and $\hat{\alpha}_e$ is the effective inclination angle modulated by the plate angular velocity. Here, the positive M is defined to induce a decrease of $\hat{\alpha}$. For an inclined bent plate, the effective wind speed U_e is taken as the velocity component normal to the plate span (figure 7*a*), whereas the modified inclination angle at the equilibrium ($\hat{\alpha}_s$) is defined between U_e and the normal vector $\boldsymbol{n}$ of the plate surface at the equilibrium bending position, as follows:

$$\left.\begin{aligned} U_e &= U_0\sqrt{1-\cos^2\alpha\,\sin^2\theta}, \\ \sin\hat{\alpha}_s &= \frac{\sin\alpha}{\sqrt{1-\cos^2\alpha\,\sin^2\theta}}. \end{aligned}\right\} \tag{3.3}$$

The effective inclination angle $\hat{\alpha}_e$ is influenced by the instantaneous angular velocity of the plate. Following the linear quasi-steady analysis characterizing the torsional instability (Païdoussis, Price & De Langre 2010), we consider an instant where the plate is in a given $\hat{\alpha}$ with an instantaneous angular velocity $\mathrm{d}\hat{\alpha}/\mathrm{d}t$ (figure 7*b*). To represent the varying relative flow velocity along the width, we define a reference radius $b\xi$ such that the plate velocity is considered as $v = (\mathrm{d}\hat{\alpha}/\mathrm{d}t)b\xi$ of the cross-section (Slater 1969; Blevins 1990) and assumed to undergo minor variations within the investigated inclination angles (Tadrist *et al.* 2015). This leads to the relative wind velocity ($\boldsymbol{U}_{rel}$) and effective inclination angle as

$$\left.\begin{aligned} \boldsymbol{U}_{rel} &= \boldsymbol{U}_e - \boldsymbol{v}, \\ \hat{\alpha}_e &= \hat{\alpha} - \gamma. \end{aligned}\right\} \tag{3.4}$$

For relatively small γ (small plate velocity compared to U_e) and low-amplitude twisting around the equilibrium,

$$\left.\begin{aligned} U_{rel} &\simeq U_e, \\ \gamma &\simeq \frac{v}{U_e}\sin\hat{\alpha} \simeq \frac{v}{U_e}\sin\hat{\alpha}_s, \end{aligned}\right\} \tag{3.5}$$

and, therefore,

$$\hat{\alpha}_e = \hat{\alpha} - \frac{\xi b}{U_e}\frac{\mathrm{d}\hat{\alpha}}{\mathrm{d}t}\sin\hat{\alpha}_s. \tag{3.6}$$

Then, using Taylor's expansion, the moment coefficient can be approximated as

$$C_M\Big|_{\hat{\alpha}_e} = C_M\Big|_{\hat{\alpha}_s} + \frac{\partial C_M}{\partial\alpha}\Big|_{\hat{\alpha}_s}(\hat{\alpha}_e - \hat{\alpha}_s). \tag{3.7}$$

The condition leading to the sudden increase of twisting motion denotes the loss of the system stability, which occurs when damping vanishes, i.e. the terms in $\mathrm{d}\hat{\alpha}/\mathrm{d}t$ (combining (3.2), (3.6) and (3.7)) are zero:

$$\frac{\partial C_M}{\partial\alpha}\Big|_{\hat{\alpha}_s} U_e \sin\hat{\alpha}_s = \frac{2c_w}{\xi b^2\rho_f A} = C, \tag{3.8}$$

where C is a constant. Key for evaluating the model is the estimation of the plate tip bending angle θ and, thus, $\hat{\alpha}_s$ at each Ca_c. Despite the variation of α, the equilibrium tip height resulted very close at a given Ca within $Ca < Ca_c$ (see example in figure 7*c*), indicating similar plate bending; therefore, θ can be inferred from the case with $\alpha = 0$ at each Ca_c directly from the PTV measurements. To determine $\partial C_M/\partial\alpha|_{\hat{\alpha}_s}$, the aerodynamic torque of a rigid metallic plate with the same geometry of the elastic counterpart was measured across various α as shown in figure 7(*d*), where the distribution of C_M follows a power-law function with α (see dashed line with power 1/2). Noting that $Ca \propto U_0^2$ for a given structure and combing (3.3) and (3.8), we can then define a dimensionless quantity C_t characterizing the threshold of Ca_c:

$$C_t = \frac{\partial C_M}{\partial\alpha}\Big|_{\hat{\alpha}_s}\sqrt{Ca_c}\sin\alpha. \tag{3.9}$$

Additional experiments were conducted to test equation (3.9), with the plate under various α. As shown in figure 8, Ca_c decreased monotonically with α; remarkably, $C_t \approx 0.2 \pm 0.005$ across all investigated α. It is worth pointing out that, compared to previous studies with rigid structures (Larsen 2002; Païdoussis *et al.* 2010; Fernandes & Armandei 2014), $\hat{\alpha}_s$ accounts for the influence of plate flexibility on the onset of twisting motions. As indicated in (3.3), strong plate deformation (i.e. large bending angle θ) leads to significant deviation of $\hat{\alpha}_s$ from the base inclination angle α, and therefore different local $\partial C_M/\partial\alpha$ due to the nonlinear dependence of C_M with α (figure 7*d*). Also, it should be noted that, for flexible plates with different geometry and material, the parameters on the right-hand side of (3.8) may vary and lead to different C_t; however, the critical Ca_c should still follow (3.9) for a given structure. That is, the abrupt force fluctuations are triggered by instability mechanisms in an inclined bent plate relative to the mean flow.

4. Conclusions

Overall, we have shown the distinctive force fluctuations and dynamics of inclined flexible plates under various flows. Our experiments revealed a sharp increase of the unsteady force, where the plate tip motions shifted from small-amplitude fluttering to twisting oscillations past a critical Ca. Further increase of the incoming velocity or Ca under sufficiently large α led to distinctive 3D orbital dynamics induced

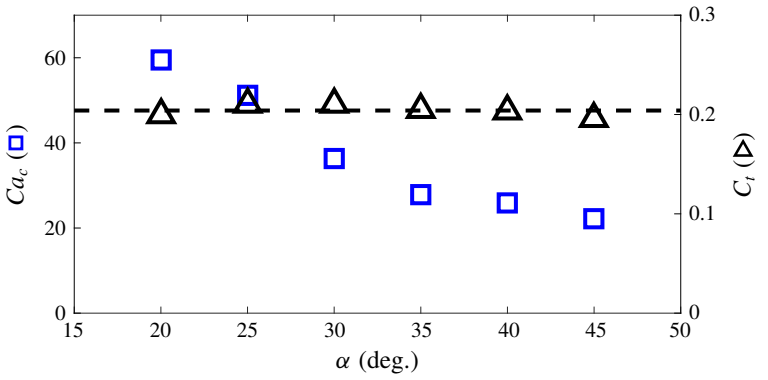

FIGURE 8. (Colour online) Ca_c and dimensionless quantity C_t (3.9) characterizing the threshold of twisting motions; the dashed line marks the averaged value of C_t across α.

by the coupled twisting and bending deformations. The agreement between our theoretical arguments and experiments demonstrates the dominating role of the dynamic instability in triggering twisting oscillations. These findings provide novel insights for examining the reconfiguration and, particularly, the large-amplitude 3D orbital motions of elastic structures under complex flow fields. Theoretical inspection of the onset of abrupt force fluctuations may be used to determine conditions for structure fatigue and design various engineering structures and processes exposed to flows. Future work will focus on the effects of mass ratio, plate geometry and other parameters in the structure dynamics and induced flow.

Acknowledgements

This work was supported by the Department of Mechanical Science and Engineering, University of Illinois at Urbana-Champaign, as part of the start-up package of L.P.C.

Supplementary movies

Supplementary movies are available at https://doi.org/10.1017/jfm.2019.40.

REFERENCES

ADRIAN, R. J., MEINHART, C. D. & TOMKINS, C. D. 2000 Vortex organization in the outer region of the turbulent boundary layer. *J. Fluid Mech.* **422**, 1–54.

ALBEN, S., SHELLEY, M. & ZHANG, J. 2002 Drag reduction through self-similar bending of a flexible body. *Nature* **420** (6915), 479–481.

ALBEN, S., SHELLEY, M. & ZHANG, J. 2004 How flexibility induces streamlining in a two-dimensional flow. *Phys. Fluids* **16** (5), 1694–1713.

ALBEN, S. & SHELLEY, M. J. 2008 Flapping states of a flag in an inviscid fluid: bistability and the transition to chaos. *Phys. Rev. Lett.* **100** (7), 074301.

AMANDOLESE, X., MICHELIN, S. & CHOQUEL, M. 2013 Low speed flutter and limit cycle oscillations of a two-degree-of-freedom flat plate in a wind tunnel. *J. Fluids Struct.* **43**, 244–255.

BHATI, A., SAWANNI, R., KULKARNI, K. & BHARDWAJ, R. 2018 Role of skin friction drag during flow-induced reconfiguration of a flexible thin plate. *J. Fluids Struct.* **77**, 134–150.

BLEVINS, R. D. 1990 *Flow-Induced Vibration*. Van Nostrand Reinhold.

FAGE, A. & JOHANSEN, F. C. 1927 On the flow of air behind an inclined flat plate of infinite span. *Proc. R. Soc. Lond.* A **116** (773), 170–197.

FERNANDES, A. C. & ARMANDEI, M. 2014 Phenomenological model for torsional galloping of an elastic flat plate due to hydrodynamic loads. *J. Hydrodyn.* **26** (1), 57–65.

GOSSELIN, F., DE LANGRE, E. L. & MACHADO-ALMEIDA, B. A. 2010 Drag reduction of flexible plates by reconfiguration. *J. Fluid Mech.* **650**, 319–341.

IVERSEN, J. D. 1979 Autorotating flat-plate wings: the effect of the moment of inertia, geometry and Reynolds number. *J. Fluid Mech.* **92** (02), 327–348.

JIA, L.-B. & YIN, X.-Z. 2008 Passive oscillations of two tandem flexible filaments in a flowing soap film. *Phys. Rev. Lett.* **100** (22), 228104.

JIN, Y. & CHAMORRO, L. P. 2017 Passive pitching of splitters in the trailing edge of elliptic cylinders. *J. Fluid Mech.* **826**, 363–375.

JIN, Y., HAYAT, I. & CHAMORRO, L. P. 2017 Modulation of aerodynamic force on a 2D elliptic body via passive splitter pitching under high turbulence. *J. Fluids Struct.* **74**, 205–213.

JIN, Y., JI, S., LIU, B. & CHAMORRO, L. P. 2016 On the role of thickness ratio and location of axis of rotation in the flat plate motions. *J. Fluids Struct.* **64**, 127–137.

JIN, Y., KIM, J.-T. & CHAMORRO, L. P. 2018*a* Instability-driven frequency decoupling between structure dynamics and wake fluctuations. *Phys. Rev. Fluids* **3**, 044701.

JIN, Y., KIM, J.-T., MAO, Z. & CHAMORRO, L. P. 2018*b* On the couple dynamics of wall-mounted flexible plates in tandem. *J. Fluid Mech.* **852**, R2.

KIM, J.-T., KIM, D., LIBERZON, A. & CHAMORRO, L. P. 2016 Three-dimensional particle tracking velocimetry for turbulence applications: case of a jet flow. *J. Visual Exp.* (108), e53745.

KIM, S., HUANG, W.-X. & SUNG, H. J. 2010 Constructive and destructive interaction modes between two tandem flexible flags in viscous flow. *J. Fluid Mech.* **661**, 511–521.

LAM, K. M. 1996 Phase-locked eduction of vortex shedding in flow past an inclined flat plate. *Eur. J. Mech. (*B*/Fluids)* **8** (5), 1159–1168.

LAM, K. M. & LEUNG, M. Y. H. 2005 Asymmetric vortex shedding flow past an inclined flat plate at high incidence. *Eur. J. Mech. (*B*/Fluids)* **24**, 33–48.

LARSEN, A. 2002 Torsion galloping of elongated bluff cross sections. In *ASME 2002 International Mechanical Engineering Congress and Exposition*, pp. 403–409. American Society of Mechanical Engineers.

LECLERCQ, T. & DE LANGRE, E. 2016 Drag reduction by elastic reconfiguration of non-uniform beams in non-uniform flows. *J. Fluids Struct.* **60**, 114–129.

LECLERCQ, T., PEAKE, N. & DE LANGRE, E. 2018 Does flutter prevent drag reduction by reconfiguration? *Proc. R. Soc. Lond.* A **474** (2209), 20170678.

LIU, B., HAMED, A. M., JIN, Y. & CHAMORRO, L. P. 2017 Influence of vortical structure impingement on the oscillation and rotation of flat plates. *J. Fluids Struct.* **70**, 417–427.

LU, L., GUO, X. L., TANG, G. Q., LIU, M. M., CHEN, C. Q. & XIE, Z. H. 2016 Numerical investigation of flow-induced rotary oscillation of circular cylinder with rigid splitter plate. *Phys. Fluids* **28** (9), 093604.

LUHAR, M. & NEPF, H. M. 2011 Flow-induced reconfiguration of buoyant and flexible aquatic vegetation. *Limnol. Oceanogr.* **56** (6), 2003–2017.

MIRZAEISEFAT, S. & FERNANDES, A. C. 2013 Stability analysis of the fluttering and autorotation of flow-induced rotation of a hinged flat plate. *J. Hydrodyn.* **25** (5), 755–762.

MODI, V. J., WILAND, E., DIKSHIT, A. K. & YOKOMIZO, T. 1992 On the fluid dynamics of elliptic cylinders. In *The Second International Offshore and Polar Engineering Conference*. International Society of Offshore and Polar Engineers.

ONOUE, K., SONG, A., STROM, B. & BREUER, K. S. 2015 Large amplitude flow-induced oscillations and energy harvesting using a cyber-physical pitching plate. *J. Fluids Struct.* **55**, 262–275.

PAÏDOUSSIS, M. P., PRICE, S. J. & DE LANGRE, E. 2010 *Fluid–Structure Interactions: Cross-Flow-Induced Instabilities*. Cambridge University Press.

RISTROPH, L. & ZHANG, J. 2008 Anomalous hydrodynamic drafting of interacting flapping flags. *Phys. Rev. Lett.* **101** (19), 194502.

SCHOUVEILER, L. & BOUDAOUD, A. 2006 The rolling up of sheets in a steady flow. *J. Fluid Mech.* **563**, 71–80.

SCHOUVEILER, L., ELOY, C. & LE GAL, P. 2005 Flow-induced vibrations of high mass ratio flexible filaments freely hanging in a flow. *Phys. Fluids* **17** (4), 047104.

SLATER, J. E. 1969 Aeroelastic instability of a structural angle section. PhD thesis, University of British Columbia.

TADRIST, L., JULIO, K., SAUDREAU, M. & DE LANGRE, E. 2015 Leaf flutter by torsional galloping: experiments and model. *J. Fluids Struct.* **56**, 1–10.

UDDIN, E., HUANG, W.-X. & SUNG, H. J. 2013 Interaction modes of multiple flexible flags in a uniform flow. *J. Fluid Mech.* **729**, 563–583.